Lab on a Chip

COMMUNICATION

Cite this: *Lab Chip*, 2016, **16**, 645

Received 10th October 2015,
Accepted 29th December 2015

DOI: 10.1039/c5lc01248a

www.rsc.org/loc

Deformability based sorting of red blood cells improves diagnostic sensitivity for malaria caused by *Plasmodium falciparum*†

Quan Guo,[a] Simon P. Duffy,[a] Kerryn Matthews,[a] Xiaoyan Deng,[a] Aline T. Santoso,[a] Emel Islamzada[a] and Hongshen Ma*[abc]

The loss of red blood cell (RBC) deformability is part of the pathology of many diseases. In malaria caused by *Plasmodium falciparum* infection, metabolism of hemoglobin by the parasite results in progressive reduction in RBC deformability that is directly correlated with the growth and development of the parasite. The ability to sort RBCs based on deformability therefore provides a means to isolate pathological cells and to study biochemical events associated with disease progression. Existing methods have not been able to sort RBCs based on deformability or to effectively enrich for *P. falciparum* infected RBCs at clinically relevant concentrations. Here, we develop a method to sort RBCs based on deformability and demonstrate the ability to enrich the concentration of ring-stage *P. falciparum* infected RBCs (*Pf*-iRBCs) by >100× from clinically relevant parasitemia (<0.01%). Deformability based sorting of RBCs is accomplished using ratchet transport through asymmetrical constrictions using oscillatory flow. This mechanism provides dramatically improved selectivity over previous biophysical methods by preventing the accumulation of cells in the filter microstructure to ensure that consistent filtration forces are applied to each cell. We show that our approach dramatically improves the sensitivity of malaria diagnosis performed using both microscopy and rapid diagnostic test by converting samples with difficult-to-detect parasitemia (<0.01%) into samples with easily detectable parasitemia (>0.1%).

Introduction

The ability to extensively and repeatedly deform is essential to the function of red blood cells (RBCs) as they transport oxygen and carbon dioxide throughout the body. The loss of this capability can contribute to microvascular occlusions resulting in tissue necrosis and organ failure, as observed in malaria,[1,2] sickle cell disease,[3] and thalassemia.[4] The loss of RBC deformability is particularly important in malaria because the parasite metabolizes hemoglobin into the toxic by-product, heme, which induces stiffening of the cell membrane through lipid peroxidation and cytoskeleton cross-linking.[5] Given the critical importance of RBC deformability, sorting cells based on this parameter provides a means to separate pathological cells from normal cells to improve diagnostic sensitivity, as well as to elucidate molecular processes associated pathogenesis.

Existing benchtop approaches for sorting RBCs include density gradient centrifugation[6] and flow cytometry.[7,8] The former has limited selectivity while the latter involves DNA fluorescent labeling that is often confounded by leukocyte and reticulocyte contamination, as well as auto-fluorescence and RNA non-specific staining.[8] RBCs have been biophysically separated based on size, deformability, permeability and cyto-adherence, using deterministic lateral displacement,[9,10] margination,[11,12] dielectrophoresis,[13] and surface-enhanced cyto-adherence.[14] These methods are effective when there are significant differences between target and background cells, such as for *Plasmodium falciparum* infected RBCs (*Pf*-iRBCs) at late (trophozoite and schizont) stages of infection. However, these methods are not effective when target cells are distinguished by more subtle differences, such as for *Pf*-iRBCs at the ring stage of infection, which is typically what's found in clinical blood samples.[15,16] *Pf*-iRBCs can also be isolated using magnetic attraction of biocrystallized hemozoin. This approach is very effective for isolating late stage *Pf*-iRBCs[17] and recently been shown to have some effect on early stage *Pf*-iRBCs, although only at high parasitemia.[18] None of the existing approaches, however, provide an effective method to sort RBCs based on deformability, as well as to enrich for early stage *Pf*-iRBCs at clinically relevant concentrations (<0.01%).

Micropore filtration has long been considered as a method to sort cells based on deformability. This approach

[a] *Department of Mechanical Engineering, University of British Columbia, 2054-6250 Applied Science Lane, Vancouver, BC, V6T 1Z4 Canada. E-mail: hongma@mech.ubc.ca*
[b] *Department of Urologic Science, University of British Columbia, Vancouver, BC, Canada*
[c] *Vancouver Prostate Centre, Vancouver General Hospital, Vancouver, BC, Canada*
† Electronic supplementary information (ESI) available. See DOI: 10.1039/c5lc01248a

has been used successfully to separate cancer cells from leukocytes,[19–22] as well as nucleated cells from RBCs,[23,24] but has not been able to sort ultra-soft cells like RBCs. This lack of selectivity for sorting RBCs arises from the inability to precisely control the pressure applied to each cell during the sorting process. In a standard membrane filter, the force used to deform each cell is determined by the pressure difference across the filtration microstructures, which is dictated by the sample flow rate and the hydrodynamic resistance of the filtration microstructure. As cells are captured in the filter microstructure, its hydrodynamic resistance increases in an unpredictable manner, significantly varying the filtration force applied to each cell. Additionally, prolonged contact between the cells and the filtration microstructures promotes adsorption, making it generally impossible to extract captured cells after separation. This problem is further exaggerated for *Pf*-iRBCs, which exhibit increased cyto-adherence due to exported parasite proteins on the cell surface.[25]

Here, we present a method to sort RBCs based on deformability and demonstrate the ability to enrich ring stage *Pf*-iRBCs at clinically relevant concentrations to dramatically improve the sensitivity of malaria diagnosis. Our method relies on ratchet transport created by deforming single cells through tapered constrictions using oscillatory flow, enabling continuous and perpetual fractionation of the input cell sample. The filtration microstructures remain unobstructed during the sorting process, which ensures that all cells experience a consistent filtration force. Additionally, the oscillatory flow prevents the adsorption of *Pf*-iRBCs to the filtration microstructure, enabling the extraction of target cells after separation. We show this method can enrich ring-stage *Pf*-iRBCs by >100×, therefore dramatically improving the detection limits of malaria diagnosis performed using microscopy and rapid diagnostic tests (RDTs).

Our work here derives from our previous studies of the microfluidic ratchet mechanism where we showed that 1) the force required to deform single cells through tapered constrictions are directionally asymmetrical,[26] 2) oscillatory deformation through such constrictions can produce a ratcheting transport behavior that depends on cell deformability, and 3) the potential to use this effect to sort nucleated cells based on deformability.[27] Here, we extended these principles to RBCs, which are orders of magnitude more deformable than nucleated cells.[28,29] Furthermore, in our previous implementation,[27] the cell sample must be batch loaded into the microfluidic device using membrane micro-valves, which limited the throughput to ~9000 cells per hour. Here, we developed a method to continuously sort RBCs based on deformability that extended the sample throughput to ~0.5 million cells per hour, which is sufficient to enrich for *Pf*-iRBCs at clinically relevant parasitemia.

Results

Deformability based cell sorting using microfluidic ratchets

The principle of the microfluidic ratchet mechanism involves deforming single cells through tapered constrictions significantly smaller than their diameter. The pressure required to deform the cell along the direction of taper (Fig. 1A) is less than the pressure required to deform the cell against the direction of taper (Fig. 1B).[26] Coupling this physical asymmetry with a biased oscillatory flow creates a ratcheting effect that transports certain cells unidirectionally through the constriction while preventing the transport of other cells. This transport process is selective on the basis of the cell's ability to squeeze through a microscopic constriction, which simulates the transport and sequestration of RBCs in the microvasculature. The oscillatory flow plays the critical role of minimizing contact between the cells and the microstructures to prevent clogging and fouling in order to ensure that a consistent deformation force is applied to each cell.

To sort RBCs using the microfluidic ratchet effect, a RBC sample is transported through a 2D array of micrometer-scale tapered constrictions. The openings of the constrictions are gradually decreased from the bottom row to the top row in order to test the ability of RBCs to transit through the constriction at progressively smaller pores (Fig. 1C). The cell sample is introduced at the bottom-left corner of the array and transported through the array by a vertical oscillatory flow and a constant horizontal cross flow. These flows combine to propel the cells in a zigzag diagonal path through the constriction matrix. As cells reach their limiting constriction size where they are unable to transit, they proceed horizontally between funnel rows towards the outlet. Since cells with different deformability will be restricted by different constriction sizes, the cell population are sorted based on deformability in this manner (Fig. 2). A video of the sorting process is provided in the ESI.†

Microfluidic device design

The constriction matrix used to sort RBCs consists of 35 rows and 630 columns of tapered constrictions. The pore size is constant in each row, and decreases every four rows from bottom to the top. In total, the 35 rows of constrictions consists of 9 different sizes (1.5, 1.75, 2, 2.25, 2.5, 3, 3.5, 6, and 7.5 μm), which sort the input sample based on deformability into 9 fractions in outlets O1–O9. The thickness of the constriction matrix chamber is 4.5 μm, which is sufficient to constrain RBCs in a planar configuration while still allowing them to be transported freely by fluid flow. Fluid flow in the constriction matrix is controlled by fluid flow from supporting microchannels originating from the sample inlet (SI), oscillation flow inlets (Osc1 and Osc2) and cross-flow inlet (CFI) (Fig. 1E).

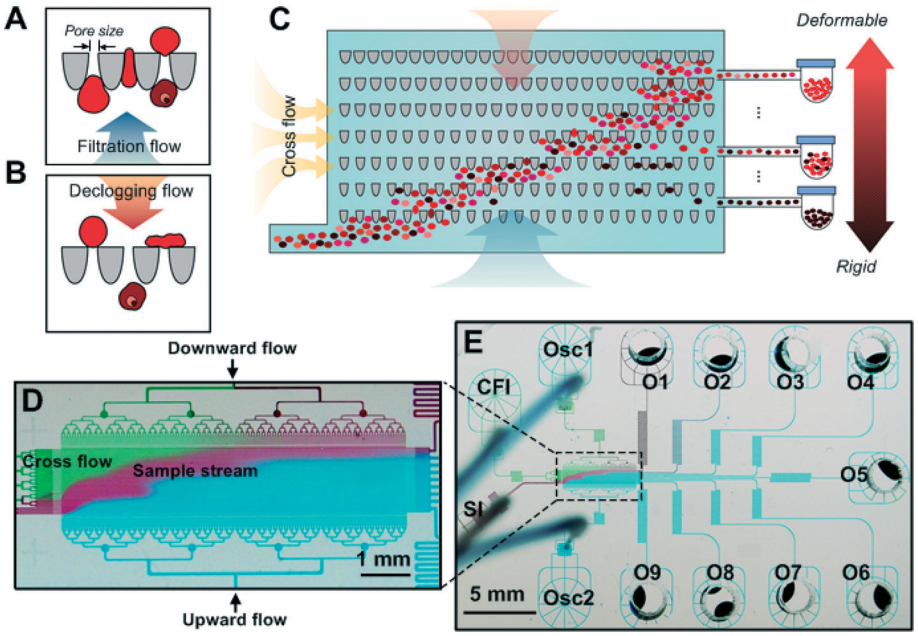

Fig. 1 Design of the ratchet-sorting device. (A–B) Tapered funnel constriction allowing unidirectional flow of cells under oscillation excitation which consists of (A) upward filtration flow and (B) downward de-clogging flow; (C) cell sorting using a matrix of funnel constrictions. The cell sample is introduced through the sample inlet (SI) and forms a diagonal trajectory under the combined forces of cross-flow inlet (CFI) and biased-oscillation flows including oscillation inlet 1 (Osc1) for declogging and oscillation inlet 2 (Osc2) for filtration. More deformable cells, such as uiRBCs, will travel further up the matrix of funnel constrictions than less deformable cells, such as *Pf*-iRBCs, which will be blocked midways and be separated from the main population. (D) Image of microfluidic ratchet device infused with different food color dyes illustrating the diagonal trajectory of the SI through the ratchet-sorting device as well the nine outlets (O1–9) constituting a deformability gradient. (E) Image of the overview design of the ratchet sorting device.

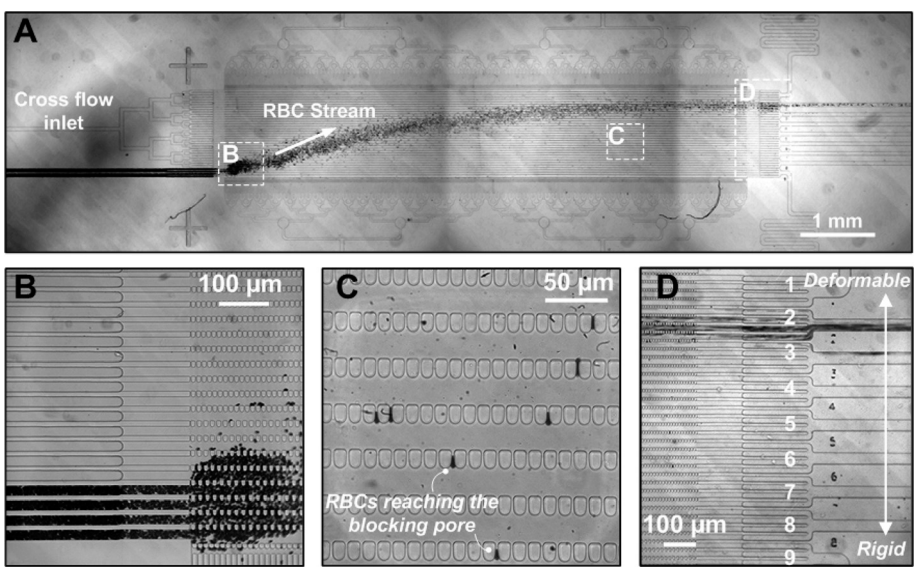

Fig. 2 Micrographs of cell sorting using the microfluidic ratchets. (A) RBCs follow a diagonal trajectory in response to the inlets flow, cross flow, and biased oscillatory flow (stitched image). (B) RBCs are introduced through the inlet, (C) transit the sorting matrix until reaching the blocking pore sizes, where (D) they proceed horizontally towards the appropriate outlet. The majority of the RBCs sample flow into the highly deformability fractions, while a minority rigid RBCs (such as *Pf*-iRBCs) are separated into the low deformability fractions.

Hydrodynamic model

Fluid flow in a microfluidic channel is linearly proportional to the drop in pressure across the length of the channel. This linear proportionality, along with the required conservation of volume of incompressible flows, allows the analysis of fluid flow using standard methods of linear electrical circuit

analysis. Specifically, the pressure and flow rate relationship can be determined from,

$$\Delta P = R_H \times Q, \quad (1)$$

where ΔP is the pressure difference across a fluidic channel, Q is the volumetric flow rate, and R_H is the hydrodynamic resistance. The hydrodynamic circuit for the microfluidic device includes microchannels leading to the funnel matrix originating from the cross flow inlet (R_{CFI}), sample inlet (R_{SI}), oscillation (R_{OSC}) and outlets (R_O) (Fig. S1†). Fluid flow in funnel matrix can be considered as a superposition of the vertical oscillatory flow circuit and the horizontal constant flow circuit (Fig. S2†). In the vertical circuit, the hydrodynamic resistance of the sorting matrix, $R_{SORT,V}$, can be determined by summing resistances of the individual funnel constrictions,

$$R_{SORT,V} = \frac{\sum_{i}^{n_{row}} r_i}{n_{column}}, \quad (2)$$

where n_{row} and n_{column} are the number of funnel rows and columns in the matrix, r_i is the resistance of the individual funnel and the value of each r_i is determined using finite element simulation (COMSOL multiphysics, full listing of the values of r_i, are in Table S1†). In the horizontal circuit, the hydrodynamic resistance of the sorting matrix, $R_{SORT,H}$, can be determined from the resistance of the spacing between each funnel row ($r_{spacing}$) using

$$R_{SORT,H} = \frac{r_{spacing}}{n_{spacing}}, \quad (3)$$

where $n_{spacing}$ is the number of horizontal spacings in the sorting matrix.

The supporting microchannels are designed to present a dominant hydrodynamic resistance (>50×) over that of the funnel matrix, allowing precise control of fluid flow using pressure-driven flow from the inlets (full listing of the hydrodynamic resistance values are in Table S2†). This *heavy-peripheral-light-center* hydrodynamic design provides a constant flow rate in the funnel matrix, whose resistance may vary with the number of cells in the funnel matrix, and thereby ensures that each cell experiences a nearly constant deformation pressure. This design further serves to dramatically reduce the pressure applied at the inlets to derive an attenuated version for each cell. Specifically, the pressures ranging from 14 to 20 kPa applied at the oscillation inlets are reduced to less than 10 Pa at each funnel constriction, which we determined previously was appropriate to distinguish normal RBCs and ring-stage iRBC through similarly sized microfluidic constrictions.[28,30,31]

Microfluidic device operation

Operation of the microfluidic device involves initially infusing the RBC population through the sample inlet and setting the pressures at the sample, oscillation, and cross flow inlets to produce a characteristic diagonal cell stream across the rectangular funnel array. The inlet pressure settings are determined empirically by observing the angle of the cell stream. If the oscillation pressure (Osc2) is too low, the cell sample do not have sufficient time to test each row of funnel constrictions and will exit the funnel array prematurely. If the oscillation pressure (Osc2) is too high, the cells will exit the funnel array at the upper boundary and then will not be transported to the outlets. The oscillatory cycle is set at 4 seconds upward followed by 1 second downward. The upward timing is selected to provide sufficient time for each cell to test at least one funnel constriction per cycle, while the downward timing is selected to provide sufficient time to release non-transiting cells from each constriction.

RBC deformability measurement

As preparation for deformability based sorting of RBCs, we first measured the deformability of RBCs in the contexts relevant to this study. RBCs deformability has been previously measured using bulk flow and single-cell approaches. Traditional bulk flow approaches, such as ektacytometry[32–34] and filtration,[35,36] provide the average deformability profile of a RBC population, but cannot discriminate properties in minor subpopulation of the RBC sample, such as in RBCs infected with *P. falciparum*. This challenge has motivated the development of single-cell deformability measurement techniques including optical tweezer,[37–39] hydrodynamic flow,[40,41] dielectrophoretic deformation force,[42] capillary obstruction,[43] membrane fluctuation,[44] transit time through micrometer scale constrictions,[45–47] and transit pressure through micrometer scale constrictions.[28,48] Transit pressure through micrometer scale constrictions is the approach most relevant to the current cell sorting work. Specifically, we used this approach to measure the threshold pressure required to squeeze individual healthy RBCs, chemically degraded RBCs, and *Pf*-iRBCs through constrictions size ranging from 2–5 μm, as shown in the inset image in Fig. 3A. The measured threshold deformation pressure is then converted to cortical tension using liquid drop model to provide an intrinsic measure of deformability independent of constriction and RBC geometry. Further details on this measurement technique are described in Guo *et al.* 2012 (ref. 28) and Myrand-Lapierre *et al.* 2014.[31]

Device validation

To establish the ability of the ratchet mechanism to sort RBCs based on deformability, we chemically degraded RBCs by exposing them to low concentrations of glutaraldehyde (GTA), a fixative agent that induces cross-linking and stabilization of RBC membrane proteins to reduce deformability in a concentration dependent manner. We verified this property by measuring the deformability (as defined by their cortical tension) of normal RBCs exposed to 0.005% to 0.025% GTA (Fig. 3A). GTA concentrations greater than 0.025% will make

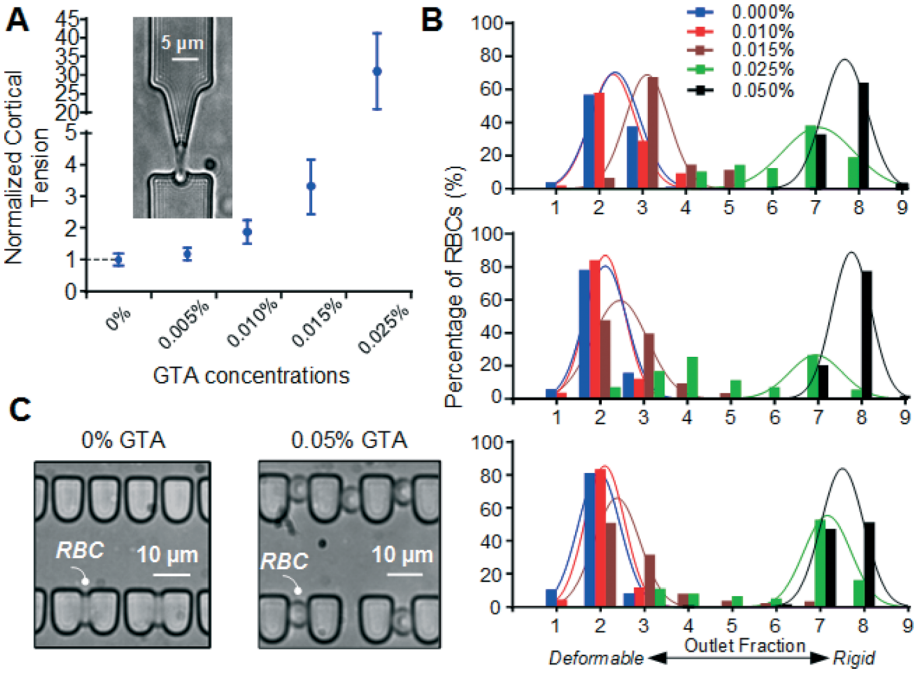

Fig. 3 Validation of deformability-based cell sorting using microfluidic ratchets. (A) Comparison of deformability of RBCs rigidified by GTA at progressively increasing concentrations; (B) normalized distributions across the outlets of the RBCs treated with various concentration of GTA for RBCs from three different donors. (C) Micrographs of 0% and 0.05% GTA treated RBCs in the funnel constrictions.

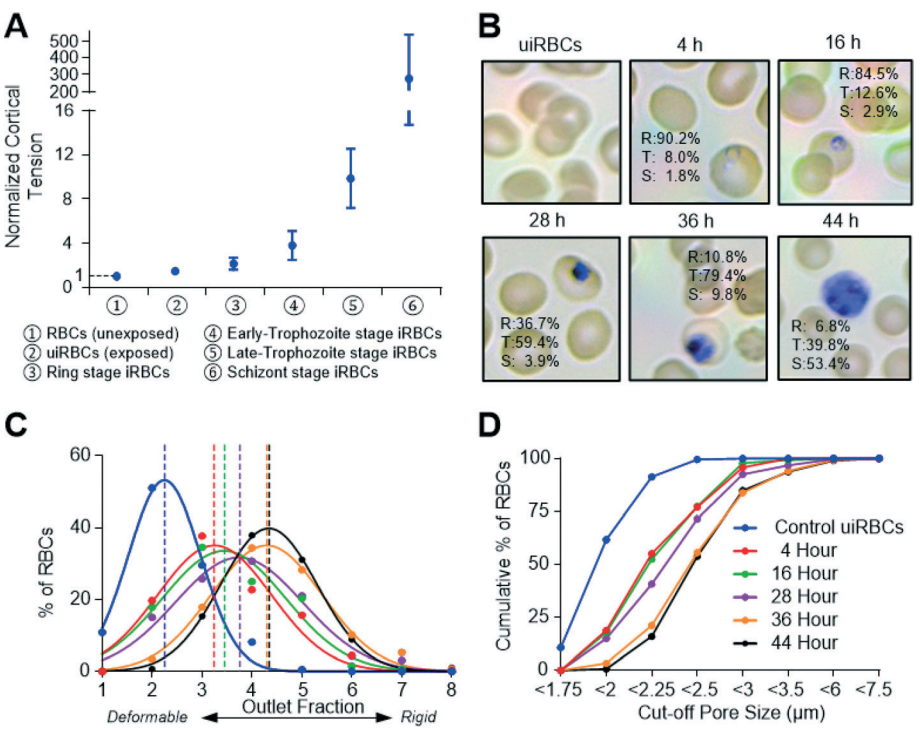

Fig. 4 Deformability-based sorting of *Pf*-iRBCs at different intra-erythrocyte stages. (A) The deformability of freshly-drawn RBCs unexposed to parasite culture, exposed but uninfected RBCs (uiRBCs) from a *P. falciparum* culture, as well as *Pf*-iRBCs at the ring, early trophozoite, late trophozoite and schizont stages (from Guo *et al.* 2012 (ref. 28)). (B) Micrographs of Giemsa stained uiRBC and *Pf*-iRBCs at 4–44 hours post-synchronization. Percentages of iRBCs at ring (R), trophozoite (T) and schizont (S) stages at each time point are shown within the images. (C) Normalized distribution of uiRBCs and *Pf*-iRBCs at 4–44 hours after ring-stage synchronization. (D) Result in C shown as cumulative distribution.

RBCs entirely rigid and unable to be deformed through the constriction at the maximum available pressure.

We then sorted RBCs exposed to 0% to 0.05% GTA. The sorting process distributed these cells into the outlets in a manner consistent with their decreased deformability. Specifically, RBCs exposed to 0.000% and 0.010% GTA were distributed in outlets 1 to 3, while increasing the GTA concentration to 0.015%, 0.025%, and 0.05% resulted in progressive rightward shifts in their distribution (Fig. 3B). RBCs exposed to 0.05% GTA retained their discoid shape even when deformed, which prevented them from transiting through 6 μm pores. This sorting experiment was repeated three times using RBCs from three different donors. The resulting RBC distributions were consistent and demonstrated the repeatability of the deformability based sorting process.

Deformability based sorting of *Pf*-iRBCs

The deformability of *Pf*-iRBCs at different intra-erythrocyte stages was measured previously to provide an estimate of their distribution after sorting (Fig. 4A).[28] We tested the potential to sort *Pf*-iRBCs at different intra-erythrocyte stages of development using synchronized *Pf*-iRBCs (see Material and methods). Aliquots from a *P. falciparum* culture at 4, 16, 28, 36, 44 hours post-synchronization were sorted and then counted (Fig. 4B). Prior to processing, each sample is stained using Hoechst DNA stain to facilitate enumeration of the *Pf*-iRBCs after sorting. Uninfected RBCs incubated in the identical environment as the parasite culture were used as a control. These cells were primarily distributed in outlets 1–4. At the 4 and 16 hour time points, *Pf*-iRBCs were predominantly at ring-stage and had a distribution centered around outlet 3. At the 28, 36, and 44 hour time points, the *Pf*-iRBCs were predominantly trophozoite and schizont stage, and had a distribution centered around outlets 4 and 5. In general, the *Pf*-iRBC distribution exhibited a monotonic rightward shift directly correlated incubation time after synchronization (Fig. 4C), which can be better visualized as a cumulative distribution (Fig. 4D). The ability to distinguish *Pf*-iRBCs at different stages of development could likely be improved by further optimization of the geometries of the constriction matrix (constriction width and thickness), as well as the filtration pressure. Nonetheless, these results are consistent with our previous efforts to measure the deformability of *Pf*-iRBCs at different stages of intra-erythrocyte development.[28]

Improving the sensitivity of microscopy based malaria diagnosis

We studied the potential to use deformability based cell sorting to enrich for *Pf*-iRBCs to improve the sensitivity of malaria diagnosis performed using microscopy. To model clinical samples, *Pf*-iRBCs synchronized at the ring-stage with approximately 5% parasitemia were doped into uninfected RBCs to create the desired parasitemia. Initially, we sorted samples at a moderately low parasitemia (0.01–0.1%) in order to determine the outlets distribution of *Pf*-iRBCs. *Pf*-iRBCs were significantly enriched in outlets 4–7 and depleted in outlets 1–3 (Fig. 5A).

To investigate the enrichment of ring-stage *Pf*-iRBCs at low parasitemia, a series of samples with parasitemia ranging from 0.04% to 0.0004% were prepared and sorted. Fractionated samples collected from outlets 4–7 were pooled together to measure the resulting parasitemia. Samples with starting parasitemia orders of magnitude lower than the detection limits of thin-film and thick-film microscopy were enriched to a detectable range (1–3% parasitemia, Fig. 5B), equivalent to enrichment factors of 100× to 2500× (Fig. 5C). The uninfected RBCs sorted into outlets 4–7 are likely to be RBCs that experience a loss of deformability resulting from natural aging and senescence,[49–51] as well as from exposure to heme by-products released from *Pf*-iRBCs.[5] The latter effect is likely responsible for the observed relationship between enrichment and initial parasitemia, where the sorting process provides greater enrichment for samples with lower initial parasitemia (Fig. 5D). Regardless of these effects, however, our results show that deformability-based ratchet sorting is able to dramatically lower the detection limit of malaria diagnosis performed using microscopy.

Improving the sensitivity of rapid diagnostic tests

Finally, we investigated the potential to use deformability based cell sorting to improve the sensitivity of malaria diagnosis performed using rapid diagnostic tests (RDT). RDT strips based on plasmodium lactate dehydrogenase (pLDH) were selected because of their low false positive rate.[52] We evaluated RDT sensitivity over a range of parasitemia and established their detection limit to be 0.004% parasitemia (Fig. 6B). We then prepared ring-stage *Pf*-iRBC samples at 0.003% and 0.0006% parasitemia, as well as a positive control at 0.1% parasitemia. The RDT was not able to detect the infection without enrichment, whereas the enriched output pooled from outlets 4–7 of the microfluidic device were detected. In these cases, the optical density of the detection band for the enriched samples were similar to 0.02% or 0.01% parasitemia respectively (Fig. 6C). These results confirm that microfluidic enrichment could dramatically increase the sensitivity of RDTs for *falciparum* malaria.

Discussion

Reduced RBC deformability is central to the pathology of *falciparum* malaria. Consequently, deformability based sorting represents a fundamental approach that could be used to enrich for pathological cells to improve diagnostic sensitivity or to fractionate these cells for further study. However, deformability based sorting of RBCs has not been previously achieved because of the extreme softness of these cells, which requires exquisite control of the deformation force applied to each cell in order to alter its flow path. The microfluidic ratchet mechanism provides a means to continuously filter sample cells without allowing them to arrest and accumulate in the filtration microstructure. This approach

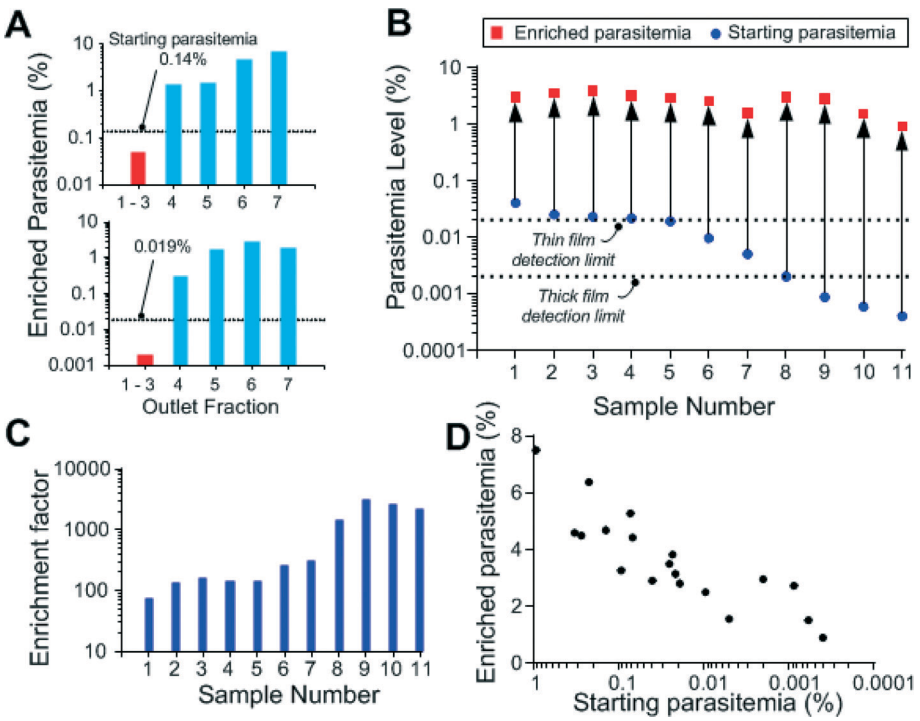

Fig. 5 Deformability based sorting of RBCs improves the sensitivity of malaria diagnosis performed using microscopy. (A) The distribution of *Pf*-iRBCs in low-parasitemia samples after sorting by the microfluidic ratchet. *Pf*-iRBCs selectively accumulate in outlets 4–7 and can achieve an increasingly greater magnitude of enrichment for samples with a low starting parasitemia (indicated by dotted line). (B) Enrichment of *Pf*-iRBC from 11 samples with parasitemia ranging from 0.04% to 0.0004%. The output sample was pooled from outlets 4–7. The initial and enriched parasitemia is shown relative to the detection limit for thin and thick film microscopy. (C) The resulting enrichment factors from the 11 samples. (D) Dot plot showing the correlation between the initial parasitemia and the enriched parasitemia.

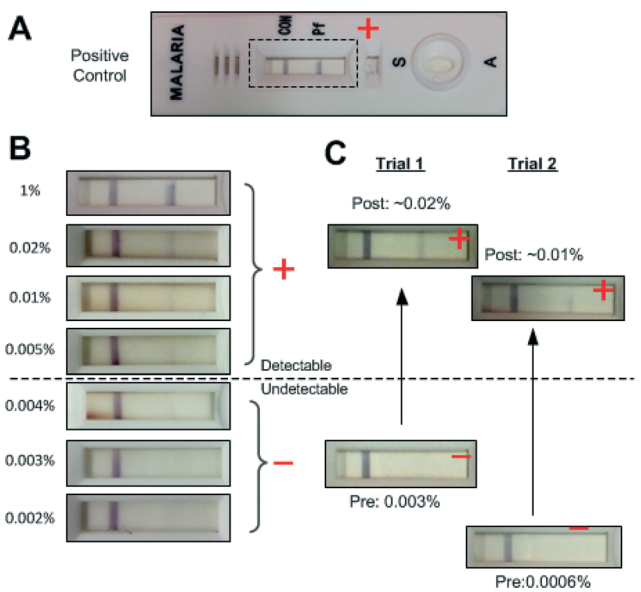

Fig. 6 Deformability based sorting of RBCs improves the sensitivity of malaria diagnosis performed using RDTs. (A) Example of malaria RDT indicating a positive result. (B) Titration of RDT result as a function of parasitemia showing the indicator band become undetectable at <0.005% parasitemia. (C) Following microfluidic enrichment of parasitized cells, samples with undetectable parasitemia (0.003% and 0.0006%) where enriched to detectable parasitemia (estimated as 0.02% and 0.01% respectively).

ensures that a consistent filtration force is applied to each cell, enabling highly selective sorting without immobilizing cells on the filter.

Deformability-based sorting could overcome a key challenge associated with the detection of malaria infection at low parasitemia in early stage infection and asymptomatic individuals. While existing high-sensitivity malaria detection methods involve PCR-based analyses[53] that require specialized laboratory infrastructure, the ability to biophysically enrich for infected RBCs by 100× (and potentially up to 2500×) could effectively lower the limit of detection for malaria diagnosis performed using conventional microscopy and RDT methods. Furthermore, microfluidic enrichment could be used to develop simple diagnosis platforms based on automated microscopy,[54,55] where existing methods are currently limited by error rate and throughput.

Finally, since change in iRBC deformability is directly correlated with parasite development and maturation, successful fractionation of *Pf*-iRBCs at various development stages could potentially aid the discovery of biomarkers associated with parasite growth and drug metabolism through RNA sequencing and proteomics. In addition to malaria, this approach could potentially be used to discover the underlying molecular mechanisms in sickle cell disease[56] and RBC senescence[57] where RBC deformability is thought to play a central role.

Material and methods

Microfluidic fabrication

Photolithography. The microfluidic ratchet device consists of a single fluidic layer fabricated using soft-lithography of polydimethylsiloxane (PDMS) silicone. Mold for the microstructure consists of two photo-lithographically defined layers fabricated on a silicon wafer. The funnel matrix was fabricated using SU-8 3005 photoresist (MicroChem, Newton, MA, USA) thinned with cyclopentanone at a ratio of 1 : 0.8 by volume. The supporting microfluidic channels were made from SU-8 3010 photoresist. The patterns for both masks were drawn using Solidworks DWG Editor.

The SU-8 3005 microstructures were fabricated on a cleaned 100 mm silicon wafer. After dehydration baking on a hotplate at 200 °C for 5 minutes, thinned SU-8 3005 was spread onto the wafer at 500 rpm for 10 seconds, and then spun at 4000 rpm for 30 seconds to remove the edge beads. The wafer was then soft baked at 95 °C on the hot plate for 20 minutes before being exposed to UV light in a mask aligner for 30 seconds. The exposed wafer was given a post exposure bake in the sequence of 65 °C for 1 minute, 95 °C for 1.5 minute and then 65 °C for 1 minute. The wafer was then developed using SU-8 developer (MicroChem). The geometry of the SU-8 3005 photoresist was stabilized by further baking on a hotplate where the temperature was gradually ramped from 40 °C to 200 °C, held at 200 °C for one hour, and then gradually cooled to 40 °C. The finished SU-8 structure was measured to be 4.5 μm in thickness using profilometer (Alpha Step 200).

The SU-8 3010 microstructures were added to the silicon wafer containing the SU-8 3005 microstructures. SU-8 3010 photoresist was spin-coated on the wafer at 3000 rpm for 50 seconds, and then at 4000 rpm for 2 seconds. The coated wafer was soft baked on hotplates set at 65 °C for 1 minute, 95 °C for 2 minutes, and then 65 °C for 1 minute. The designed mask for the SU-8 3010 pattern was then aligned with the SU-8 3005 pattern and exposed for 4 minutes in 30 seconds bursts. After waiting for approximately 30 minutes, the wafer was developed using SU-8 developer (MicroChem). The finished structure was measured to be 10 μm in thickness using profilometer (Alpha Step 200).

Soft-lithography. Replicas of the silicon wafer molds were fabricated using a polyurethane-based plastic (Smooth-Cast ONYX SLOW, Smooth-On) using the process described by Desai.[58] PDMS microfluidic devices were then fabricated from these molds using soft-lithography of RTV 615 PDMS (Momentive Performance Materials).

After baking, the cured microfluidic device was removed from its mold, and holes were punched into it using a 0.5 mm outer diameter hole punch (Technical Innovations, Angleton, TX, USA) as the fluidic introduction ports including cross flow and cell inlets as well as the oscillation inlets. The outlets are punched using 4 mm diameter puncher. The microfluidic device is then bonded to a blank layer of PDMS spin-coated onto a blank silicon wafer at 1500 rpm for 1 minutes. The device containing a blank layer of PDMS at bottom is then peeled off. The bonding is realized through the exposure of both surfaces to oxygen plasma (Model PDC-001, Harrick Plasma) for 70 seconds before the PDMS device is brought into contact with the blank PDMS layer to create a permanent covalent bond. After peeled off from the wafer, the double layer device is subsequently bonded to the standard microscope slide (Fisher Scientific) cleaned beforehand with acetone and isopropanol.

Blood preparation

Normal packed RBCs. From healthy donors was obtained *via* venipuncture in tube containing EDTA anti-coagulant, following informed consent and approval from the University of British Columbia (UBC) Research Ethics Board. The whole blood was spun down at 3000 g for 10 minutes. The plasma, the buffy coat and the top layer of the cells were then removed. The remaining cells are normal packed RBCs. For the glutaraldehyde study, the packed RBCs were used within the same day. Packed RBCs were also used to feed the *Plasmodium falciparum* parasites.

Glutaraldehyde treatment. Packed RBCs were suspended in Phosphate Buffered Saline (PBS; $CaCl_2$-free and $MgSO_4$-free; Invitrogen) with 0.2% Pluronic™ F-127 (Invitrogen). Diluted RBCs were incubated for 30 minutes at 25 °C with 0 to 0.05% glutaraldehyde (GTA; Alfa Aesar, MA). After incubation, the RBCs suspension was washed three times in PBS and then re-suspended in PBS with 0.2% Pluronic.

***P. falciparum* culture and ring stage synchronization.** The 3D7 strain of *P. falciparum* parasites was cultured under standard *in vitro* conditions with modifications.[59] Type A+ blood was collected from healthy donors with written informed consent and approval from the Research Ethics Boards of UBC and Canadian Blood Services (CBS) by the CBS' Network Centre of Applied Development. Cultures were maintained at approximately 5% hematocrit in malaria culture medium (1640 RPMI with HEPES; 0.2% sodium bicarbonate; 100 μM hypoxanthine; 10% heat-inactivated human serum; 1 mg ml^{-1} gentamicin). Parasites were incubated in an atmosphere of 5% CO_2, 3% O_2 and 92% N_2 at 37 °C and 95% humidity. To achieve synchronous *falciparum* culture, 5% (w/v) sorbitol solution was dissolved thoroughly in distilled water and warmed at 37 °C for 5 minutes. Malaria culture at 50% was added to the sorbitol solution at 1 : 9 ratio. The mixture was incubated for 8 minutes at 37 °C following 30 seconds of vigorous vortex to rupture old and mature parasites. Then centrifuge the sample at 250 g for 5 minutes at 37 °C and remove the supernatant. The synchronous culture with mostly ring parasites was cleaned twice with culture medium at 250 g for 5 minutes.

Magnetic column purification. Magnetic column purification was used in conjunction with sorbitol treatment to achieve tighter synchronous sample. A magnetic purification stand was fabricated based on the design by Charles C. Kim[60] with some modifications to fit super magnets. LS

columns (Miltenyi Biotec, Bergisch Gladbach, Germany) which are designed for positive selection of strongly magnetically labeled cells were used. They were initially washed once with 5 ml incomplete RPMI medium (10.4 g l^{-1} RPMI-1640, 25 mM HEPES, 0.5% AlbuMAX I (w/v), 100 μM hypoxanthine, 12.5 μg ml^{-1} gentamicin) before loading sorbitol synchronized sample (2% hematocrit). The subpopulation trapped by the magnet was discarded while the eluted sample was transferred into a 15 ml Falcon tube (Corning Life Science, Tewksbury, MA, USA), which was washed twice by centrifuging at 2000 rpm for 5 minutes without brake.

Parasite staining processes

Giemsa staining. Blood smears of the cell cultures of approximately 50% hematocrit (asynchronous and synchronous) were prepared onto a slide. The specimens were air-dried, fixed in methanol and stained with 10% Giemsa to evaluate the stages of the infected RBCs. Parasitemia was determined by counting at least 1000 RBCs under regular light microscope, equipped with a 100× oil-immersion objective. Microscopic pictures were taken with Nikon camera mounted on the microscope. Images of the Giemsa stained *Pf*-iRBCs were shown in Fig. S3A.†

Hoechst fluorescence staining. Synchronous sample was stained with Hoechst 33342 (sigma) before introduced through the device. Hoechst (5 μg ml^{-1}) were added to the sample at roughly 20% hematocrit at 1 : 100 (v/v) in PBS solution with 2% heat-inactivated fetal bovine serum (FBS). The stained *falciparum* sample were incubated for 20 minutes in room temperature in the dark. The sample, after sorting, was observed under fluorescence microscope and images of stained *Pf*-iRBCs are shown in Fig. S3B.†

Rapid diagnostic tests (RDTs)

Rapid diagnostic tests detect malaria infection based on the presence of parasite specific antigens, which produces a color change on an absorbent test strip. The two primary antigens used to detect falciparum malaria are *Plasmodium falciparum* histidine-rich protein 2 (*Pf*HRP2) and Plasmodium lactate dehydrogenase (pLDH). *Pf*HRP2 is believed to be more sensitive but suffers from false-positives due to antigen persistence following parasite clearance. RDTs based on pLDH do not suffer from antigen persistence but are less sensitive than PfHRP2-based RDTs.[61,62] For the RDT tests, CareStart™ test strips for pLDH antigen were purchased from AccessBIO. Malaria samples containing low density ring stage *Pf*-iRBCs were tested before and after the microfluidic enrichment. Pre-sorting samples were prepared at 40% hematocrit and a 5 μl aliquot was transferred into the RDT reservoir for testing. Post-sorting samples were prepared by pooling samples from outlets 4–9 together, and then centrifuged to remove the excess supernatant. The remaining cells, suspended in 5 μl of liquid, are then transferred into the reservoir of the RDT for testing.

References

1 H. A. Cranston, C. W. Boylan, G. L. Carroll, S. P. Sutera, J. R. Williamson, I. Y. Gluzman, D. J. Krogstad, R. Williamson, I. Y. Gluzman and D. J. Krogstad, *Science*, 1984, **223**, 400–403.

2 M. Paulitschke and G. B. Nash, *J. Lab. Clin. Med.*, 1993, **122**, 581–589.

3 G. B. Nash, C. S. Johnson, H. J. Meiselman, B. Nash and C. S. Johnson, *Blood*, 1984, **63**, 73–82.

4 S. L. Schrier, *Annu. Rev. Med.*, 1994, **45**, 211–218.

5 F. Nuchsongsin, K. Chotivanich, P. Charunwatthana, O.-S. Fausta, D. Taramelli, N. P. Day, N. J. White and A. M. Dondorp, *Am. J. Trop. Med. Hyg.*, 2007, **77**, 617–622.

6 E. M. Rivadeneira, M. Wasserman and C. T. Espinal, *J. Protozool.*, 1983, **30**, 367–370.

7 S. Philipp, H.-H. Oberg, O. Janssen, M. Leippe and C. Gelhaus, *Cytometry. A*, 2012, **81**, 1048–1054.

8 G. Jun, J.-S. Lee, Y.-J. Jung and J.-W. Park, *J. Korean Med. Sci.*, 2012, **27**, 1137–1142.

9 D. Holmes, G. Whyte, J. Bailey, N. Vergara-Irigaray, A. Ekpenyong, J. Guck and T. Duke, *Interface Focus*, 2014, **4**, 20140011–20140011.

10 T. Krueger, D. Holmes and P. Coveney, *Biomicrofluidics*, 2014, **8**, 1–10.

11 H. W. Hou, A. A. S. Bhagat, A. G. L. Chong, P. Mao, K. S. W. Tan, J. Han and C. T. Lim, *Lab Chip*, 2010, **10**, 2605–2613.

12 T. M. Geislinger, S. Chan, K. Moll, A. Wixforth, M. Wahlgren and T. Franke, *Malar. J.*, 2014, **13**, 375.

13 S. Choi, J.-K. Park, P. Gascoyne, C. Mahidol, M. Ruchirawat, J. Satayavivad, P. Watcharasit and F. F. Becker, *Lab Chip*, 2002, **2**, 70–75.

14 Y.-H. Hsu, P. Lu, J. L. Coleman and W. C. Tang, *Biomed. Microdevices*, 2011, **13**, 995–1004.

15 I. Safeukui, J.-M. Correas, V. Brousse, D. Hirt, G. Deplaine, S. Mulé, M. Lesurtel, N. Goasguen, A. Sauvanet, A. Couvelard, S. Kerneis, H. Khun, I. Vigan-Womas, C. Ottone, T. J. Molina, J.-M. Tréluyer, O. Mercereau-Puijalon, G. Milon, P. H. David and P. A. Buffet, *Blood*, 2008, **112**, 2520–2528.

16 A. M. Dondorp, P. A. Kager, J. Vreeken and N. J. White, *Parasitol. Today*, 2000, **16**, 228–232.

17 F. Paul, S. Roath, D. Melville, D. C. Warhurst and J. O. S. Osisanya, *Lancet*, 1981, **318**, 70–71.

18 J. Nam, H. Huang, H. Lim, C. Lim and S. Shin, *Anal. Chem.*, 2013, **85**, 7316–7323.

19 S. Zheng, H. Lin, J.-Q. Liu, M. Balic, R. Datar, R. J. Cote and Y.-C. Tai, *J. Chromatogr. A*, 2007, **1162**, 154–161.

20 I. Desitter, B. S. Guerrouahen, N. Benali-Furet, J. Wechsler, P. A. Jänne, Y. Kuang, M. Yanagita, L. Wang, J. A. Berkowitz, R. J. Distel and Y. E. Cayre, *Anticancer Res.*, 2011, **31**, 427–441.

21 G. Vona, A. Sabile, M. Louha, V. Sitruk, S. Romana, K. Schütze, F. Capron, D. Franco, M. Pazzagli, M. Vekemans, B. Lacour, C. Bréchot and P. Paterlini-Bréchot, *Am. J. Pathol.*, 2000, **156**, 57–63.

22 X. Qin, S. Park, S. P. Duffy, K. Matthews, R. R. Ang, T. Todenhöfer, H. Abdi, A. Azad, J. Bazov, K. N. Chi, P. C. Black and H. Ma, *Lab Chip*, 2015, **15**, 2278–2286.

23 H. M. Ji, V. Samper, Y. Chen, C. K. Heng, T. M. Lim and L. Yobas, *Biomed. Microdevices*, 2008, **10**, 251–257.
24 V. VanDelinder and A. Groisman, *Anal. Chem.*, 2007, **79**, 2023–2030.
25 C. A. Moxon, G. E. Grau and A. G. Craig, *Br. J. Haematol.*, 2011, **154**, 670–679.
26 Q. Guo, S. McFaul and H. Ma, *Phys. Rev. E: Stat., Nonlinear, Soft Matter Phys.*, 2011, **83**, 051910.
27 S. M. McFaul, B. K. Lin and H. Ma, *Lab Chip*, 2012, **12**, 2369–2376.
28 Q. Guo, S. J. Reiling, P. Rohrbach and H. Ma, *Lab Chip*, 2012, **12**, 1143–1150.
29 Q. Guo, S. Park and H. Ma, *Lab Chip*, 2012, **12**, 2687–2695.
30 A. T. Santoso, X. Deng, J.-H. Lee, K. Matthews, S. P. Duffy, E. Islamzada, S. M. McFaul, M.-E. Myrand-Lapierre and H. Ma, *Lab Chip*, 2015, **15**, 4451–4460.
31 M.-E. Myrand-Lapierre, X. Deng, R. R. Ang, K. Matthews, A. T. Santoso and H. Ma, *Lab Chip*, 2014, **15**, 159–167.
32 W. Groner, N. Mohandas and M. Bessis, *Clin. Chem.*, 1980, **26**, 1435–1442.
33 S. Shin, Y. Ku, M.-S. Park and J.-S. Suh, *Cytometry, Part B*, 2005, **65**, 6–13.
34 O. K. Baskurt, M. R. Hardeman, M. Uyuklu, P. Ulker, M. Cengiz, N. Nemeth, S. Shin, T. Alexy and H. J. Meiselman, *Biorheology*, 2009, **46**, 251–264.
35 H. L. Reid, A. J. Barnes, P. J. Lock, J. A. Dormandy and T. L. Dormandy, *J. Clin. Pathol.*, 1976, **29**, 855–858.
36 J. Stuart, *J. Clin. Pathol.*, 1985, **38**, 965–977.
37 M. Dao, C. T. Lim and S. Suresh, *J. Mech. Phys. Solids*, 2003, **51**, 2259–2280.
38 K. Bambardekar, A. K. Dharmadhikari, J. A. Dharmadhikari, D. Mathur and S. Sharma, *J. Biomed. Opt.*, 2014, **13**, 064021.
39 G. Lenormand and A. Richert, *Biophys. J.*, 1999, **76**, 1145–1151.
40 S. Cha, T. Shin, S. S. Lee, W. Shim, G. Lee, S. J. Lee, Y. Kim and J. M. Kim, *Anal. Chem.*, 2012, **84**, 10471–10477.
41 D. R. Gossett, H. T. K. Tse, S. A. Lee, Y. Ying, A. G. Lindgren, O. O. Yang, J. Rao, A. T. Clark and D. Di Carlo, *Proc. Natl. Acad. Sci. U. S. A.*, 2012, **109**, 7630–7635.
42 I. Doh, W. Lee, Y. Cho, A. Pisano and F. Kuypers, *Int. Conf. Miniaturized Syst. Chem. Life Sci., 16th*, 2012, **173702**, 242–244.
43 J. P. Shelby, J. White, K. Ganesan, P. K. Rathod and D. T. Chiu, *Proc. Natl. Acad. Sci. U. S. A.*, 2003, **100**, 14618–14622.
44 Y. Park, M. Diez-Silva, G. Popescu, G. Lykotrafitis, W. Choi, M. S. Feld and S. Suresh, *Proc. Natl. Acad. Sci. U. S. A.*, 2008, **105**, 13730–13735.
45 S. Huang, A. Undisz, M. Diez-Silva, H. Bow, M. Dao and J. Han, *Integr. Biol.*, 2013, **5**, 414–422.
46 Y. Zheng, E. Shojaei-Baghini, A. Azad, C. Wang and Y. Sun, *Lab Chip*, 2012, **12**, 2560.
47 A. Adamo, A. Sharei, L. Adamo, B. Lee, S. Mao and K. F. Jensen, *Anal. Chem.*, 2012, **84**, 6438–6443.
48 Q. Guo, S. P. Duffy, K. Matthews, A. T. Santoso, M. D. Scott and H. Ma, *J. Biomech.*, 2014, **47**, 1767–1776.
49 K. Matthews, M.-E. Myrand-Lapierre, R. R. Ang, S. P. Duffy, M. D. Scott and H. Ma, *J. Biomech.*, 2015, **48**(15), 4065–4072.
50 F. H. Bosch, J. M. Werre, L. Schipper, B. Roerdinkholder-Stoelwinder, T. Huls, F. L. Willekens, G. Wichers and M. R. Halie, *Eur. J. Haematol.*, 1994, **52**, 35–41.
51 S. P. Sutera, R. A. Gardner, C. W. Boylan, G. L. Carroll, K. C. Chang, J. S. Marvel, C. Kilo, B. Gonen and J. R. Williamson, *Blood*, 1985, **65**, 275–282.
52 J. Maltha, I. Guiraud, P. Lompo, B. Kaboré, P. Gillet, C. Van Geet, H. Tinto and J. Jacobs, *Malar. J.*, 2014, **13**, 20.
53 N. Tangpukdee, C. Duangdee, P. Wilairatana and S. Krudsood, *Korean J. Parasitol.*, 2009, **47**, 93–102.
54 Y. Purwar, S. L. Shah, G. Clarke, A. Almugairi and A. Muehlenbachs, *Malar. J.*, 2011, **10**, 364.
55 M. Sheikhhosseini, H. Rabbani, M. Zekri and A. Talebi, *J. Microsc.*, 2013, **252**, 189–203.
56 M. R. Clark, N. Mohandas and S. B. Shohet, *J. Clin. Invest.*, 1980, **65**, 189–196.
57 F. H. Bosch, J. M. Werre, B. Roerdinkholder-Stoelwinder, T. H. Huls, F. L. Willekens and M. R. Halie, *Blood*, 1992, **79**, 254–260.
58 S. P. Desai, D. M. Freeman and J. Voldman, *Lab Chip*, 2009, **9**, 1631–1637.
59 W. Trager and J. B. Jensen, *Science*, 1976, **193**, 673–675.
60 C. C. Kim, E. B. Wilson and J. L. DeRisi, *Malar. J.*, 2010, **9**, 17.
61 J. C. Mouatcho and J. P. Dean Goldring, *J. Med. Microbiol.*, 2013, **62**, 1491–1505.
62 A. Moody, *Clin. Microbiol. Rev.*, 2002, **15**, 66–78.

